

A Simulation of the Effects of Receive Field Contrast on Motion-Corrected EPI Time Series

D. Sheltraw^{a,*}, B. Inglis^a

^a*Henry H. Wheeler Jr. Brain Imaging Center, University of California, Berkeley, CA, 94720, USA*

Abstract

The receive field of MRI imparts an image contrast which is spatially fixed relative to the receive coil. If motion correction is used to correct subject motion occurring during an EPI time series then the receiver contrast will effectively move relative to the subject and produce temporal modulations in the image amplitude. This effect, which we will call the RFC-MoCo effect, may have consequences in the analysis and interpretation of fMRI results. There are many potential causes of motion-related noise and systematic error in EPI time series and isolating the RFC-MoCo effect would be difficult. Therefore, we have undertaken a simulation of this effect to better understand its severity. The simulations examine this effect for a receive-only single-channel 16-leg birdcage coil and a receive-only 12-channel phased array. In particular we study: (1) The effect size; (2) Its consequences to the temporal correlations between signals arising at different spatial locations (spatial-temporal correlations) as is often calculated in resting state fMRI analyses; and (3) Its impact on the temporal signal-to-noise ratio of an EPI time series. We find that signal changes arising from the RFC-MoCo effect are likely to compete with BOLD (blood-oxygen-level-dependent) signal changes in the presence of significant motion, even under the assumption of perfect motion correction. Consequently, we find that the RFC-MoCo effect may lead to spurious temporal correlations across the image space, and that temporal SNR may be degraded with increasing motion.

*Principal corresponding author

Email address: sheltraw@berkeley.edu (D. Sheltraw)

1. Introduction

Subject motion can be a significant source of noise in BOLD (blood-oxygen-level-dependent (Ogawa et al., 1990)) functional magnetic resonance imaging (fMRI), a neuroscience research tool employing time series of gradient echo images, most commonly using the echo planar imaging (EPI) pulse sequence. This problem has been recognized since the inception of fMRI (Hajnal et al., 1994). The most obvious concern is that motion of the brain, with its contrast fixed relative to the head, will produce temporal variations at any given point in image space that can mask the BOLD or be erroneously attributed to the BOLD effect. But there can also be contrast within brain images that is fixed relative to the scanner. Such contrast can potentially be exacerbated by motion correction since following correction such contrast would then move relative to the brain and produce its own temporal variation.

With the proliferation of MRI systems employing multichannel receiver arrays (phased arrays) arises greater potential sensitivity to motion-related error and noise in EPI time series data due to scanner-fixed receiver contrast. Although multichannel receiver arrays hold great promise for improved tSNR (temporal signal-to-noise ratio) it presently appears that motion-related noise may be limiting their usefulness (Hartwig et al., 2011). The effects of motion can be especially problematic when accelerated imaging (Griswold et al., 2002; Pruessmann et al., 1999) is used in EPI time series (Sheltraw et al., 2012). However, even in the absence of acceleration there are many potential motion-related effects that can prevent multichannel receiver arrays from achieving their motion-free tSNR potential. One such effect, arising from scanner-fixed contrast, which we will call the RFC-MoCo effect (Receive Field Contrast Motion Correction effect), may occur when motion correction is applied to EPI time series data possessing significant receive field contrast.

There are many potential causes of motion-related noise in EPI time series. Here are some of the acknowledged important sources of noise and systematic error in non-accelerated EPI:

1. Poor motion correction: Most motion correction algorithms used in fMRI (Cox, 1996; Friston et al., 1995; Smith et al., 2001; Woods et al., 1991) assume that a volume of image slices moves as a rigid body. Since a volume of data is usually collected over a time interval of 1 to 2 seconds there is clearly enough time for the head to move during such an interval, thereby violating the rigid volume assumption. This may lead to bad estimates of motion parameters and inadequate correction of motion-related contrast

fluctuations. Furthermore the issue is often complicated by the use of additional temporal interpolation (Roche, 2011; Bannister et al., 2007) as well.

2. Spin history: The steady state of the pre-excitation magnetization, established after a few TR (repetition time) periods in the absence of motion, is perturbed by motion orthogonal to the imaging planes of 2D multislice EPI (Muresan et al., 2005), potentially causing increased noise and systematic effects upon spatial-temporal correlations.
3. Main field inhomogeneity: The presence of an object within the strong main magnetic field B_0 of MRI leads to increased inhomogeneity of the field. The inhomogeneity results in image distortions which increase in severity with field strength (Jezzard and Balaban, 1995). Shim coils are used to try to restore field homogeneity but shim coils are fundamentally limited with respect to the fields they can compensate. When the object moves the inhomogeneity varies with respect to time which may potentially increase noise and systematic error in the time series images while decreasing image-space signal strength.
4. Receive field distortion: A receiver coil loaded with a head will distort the coil's receive field (Giovannetti et al., 2008). This distortion should be more pronounced at high main field strengths (Wiesinger et al., 2006). As the head moves this distortion will vary in time thereby adding temporal fluctuations in an EPI time series.
5. RFC-MoCo effect: The receive field, when not spatially homogeneous, will impose an image contrast that is fixed relative to the scanner (Hartwig et al., 2011). When an assumed perfect motion correction is applied to a time series of such images the receive field effectively moves relative to the imaged object. This temporally varying image contrast may potentially produce tSNR degradation and systematic effects upon spatial-temporal correlations.
6. TFC-MoCo effect: The transmit field, when not spatially homogeneous, will also impose an image contrast that is fixed relative to the scanner and will produce temporally varying image contrast in a motion-corrected time series of images in a manner analogous to the RFC-MoCo effect. Most commercial scanners used in fMRI research today make use of a large diameter birdcage body coil to produce the transmit field. The large diameter, as compared to a head coil, increases the transmit field homogeneity and therefore decreases the potential TFC-MoCo effect.

The RFC-MoCo effect is the focus of this paper. In particular, we seek to estimate the effect size of tSNR degradation and any spurious spatial-temporal

correlations induced by the receive field contrast. This is an important subject because there is a small handful of reports of little benefit arising from use of a 32-channel coil for fMRI, compared to a 12-channel coil (Hartwig et al., 2011; Kaza et al., 2009, 2011; Li et al., 2009), and we have received anecdotal reports of poorer performance of the 32-channel coil for fMRI in our own center. Thus, we were motivated to investigate the RFC-MoCo effect because of a suspicion that it may produce a limiting motion sensitivity when compared to the same protocol acquired with a smaller phased array coil. Furthermore, recent reports (Van Dijk et al., 2012; Power et al., 2011) have suggested that a significant (but unknown) fraction of correlations determined in resting-state functional connectivity (RS-FC) studies are driven by head motion. We hypothesized that the RFC-MoCo effect could be a cause of such errors, given the use of phased array coils for the majority of RS-FC fMRI studies to date.

The use of a prescan normalization as a means for correcting the RFC-MoCo effect has been studied by Hartwig et al. (Hartwig et al., 2011). Also Kaza et al. (Kaza et al., 2009) used prescan-normalized and unnormalized data in a comparison of fMRI efficacy using 12-channel and 32-channel phased array coils. However, experimentally isolating the RFC-MoCo effect from the other potential causes of motion-related effects in time-series EPI would be very difficult if not impossible. Therefore in this paper we undertake simulations of the RFC-MoCo effect, which by design incorporates an assumption of perfect motion correction, that will allow us to elucidate the effect’s impact upon EPI time series data.

When choosing a receive coil for fMRI it is important to assure that the subject within the coil will have visual access to stimuli or cues presented on a screen placed outside the coil. Commercially available 12-channel arrays give good visual access for fMRI applications and are widely used. A birdcage coil with sixteen legs will give comparable visual access to that of the 12-channel array consisting of the usual overlapping coil elements. This specification motivates our choice of coil geometries in our simulations. In this paper we carry out simulations of the RFC-MoCo effect for: (1) A 12-channel head coil receive array consisting of 12 independent coil elements with a cylindrical geometry similar to those commonly used in modern scanners; and (2) A 16-leg receive-only birdcage head coil. In particular we will simulate: (1) The RFC-MoCo effect size; (2) A spatial map of temporal correlations due to the RFC-MoCo effect with respect to a seed point (as is often calculated in resting state fMRI analyses); and (3) The tSNR of an EPI time series when the noise of the RFC-MoCo effect is present in addition to the usual Gaussian noise of the complex-valued images.

2. Theory

The use of multichannel receiver arrays is commonplace in magnetic resonance imaging and fMRI in particular. Whether the image data is to be used in accelerated GRAPPA-like parallel imaging or non-accelerated imaging, one must combine the image data from the individual coil elements into a single composite image. Of the various methods that could be used to generate a composite image from the images generated by each coil, the sum-of-squares (SOS) method (Roemer et al., 1990) is ubiquitous. The SOS image reconstruction method creates a composite estimated image $\hat{\rho}(\mathbf{r})$ from the complex-valued images $\rho_m(\mathbf{r})$ associated with each of the M receive coils of the array by the following operation:

$$\hat{\rho}(\mathbf{r}) = \left[\sum_{m=1}^M |\rho_m(\mathbf{r})|^2 \right]^{1/2}. \quad (1)$$

Note that when $M = 1$ (a single channel) the result is the usual magnitude image associated with a birdcage coil. Equation (1) assumes that we have a representation of the image $\hat{\rho}(\mathbf{r})$ in the continuum image-space rather than a discrete image-space. In practice the image will always be in a discrete image-space which is related to the underlying continuum image-space object through a convolution with a point-spread function determined by the sampling of k -space. The discretization is expected to influence the RFC-MoCo effect upon tSNR, as well as methods to correct for the effect, but for the purpose of establishing the size and importance of the effect the use of the continuum image-space representation should be sufficient and is expected to give a best-case estimate of the size and importance of the effect in EPI time series used in fMRI.

In the absence of noise (electronic or body noise) and motion Equation (1) can be written as

$$\hat{\rho}(\mathbf{r}) = \left[\sum_{m=1}^M |\rho(\mathbf{r})c_m(\mathbf{r})|^2 \right]^{1/2} = |\rho(\mathbf{r})| \left[\sum_{m=1}^M |c_m(\mathbf{r})|^2 \right]^{1/2} \quad (2)$$

where $\rho(\mathbf{r})$ is the complex valued true image and $c_m(\mathbf{r})$ is the receive field of the m^{th} coil element of the array. Therefore the SOS method results in an image contrast which is dependent upon the array geometry and is spatially-fixed with respect to the scanner.

The imaged object ρ may undergo rigid body motion (rotation and translation) with respect to the scanner frame of reference. We denote this motion by a

time-dependent affine transformation operator $\mathcal{A}(t_n)$ where $t_n = n\Delta t$ is the time at which the n^{th} volume of image data is acquired. We will assume that the object does not move by a significant amount on a time scale less than Δt . This restriction imposes another best-case scenario on the effects of motion: Real motion is likely to occur within a TR period and will produce more complex effects, in particular spin history effects that will interact with the RFC-MoCo effect. Thus, for simplicity, we consider the RFC-MoCo effect in isolation and note that the real effects on data are likely to be worse than presented here. The SOS estimated image of the object at time t_n is then given by

$$\hat{\rho}(\mathbf{r}, t_n) = \left[\sum_{m=1}^M |c_m(\mathbf{r})\mathcal{A}(t_n)\rho(\mathbf{r}) + \eta_m|^2 \right]^{1/2} \quad (3)$$

where η_m is the uniform noise image for the m^{th} coil.¹

The usual, but idealized, motion correction is performed by applying the inverse of the affine transformation $\mathcal{A}(t_n)$ to the SOS image $\hat{\rho}(\mathbf{r}, t_n)$ to obtain the motion-corrected image $\hat{\rho}_c(\mathbf{r}, t_n)$ given by

$$\hat{\rho}_c(\mathbf{r}, t_n) = \mathcal{A}^{-1}(t_n)\hat{\rho}(\mathbf{r}, t_n) \quad (4)$$

$$= \mathcal{A}^{-1}(t_n) \left[\sum_{m=1}^M |c_m(\mathbf{r})\mathcal{A}(t_n)\rho(\mathbf{r}) + \eta_m|^2 \right]^{1/2} \quad (5)$$

$$= \left[\sum_{m=1}^M |\rho(\mathbf{r})\mathcal{A}^{-1}(t_n)c_m(\mathbf{r}) + \eta_m|^2 \right]^{1/2}. \quad (6)$$

Therefore the effect of combined motion and motion correction is mathematically equivalent to moving the receive coil elements relative to the imaged object. As explained in the Methods section this equivalence will be used to generate the time varying contrast of our simulated RFC-MoCo effect.²

To calculate the RFC-MoCo effect size, temporal correlation map, and tSNR we respectively calculate the percent difference map $D_p(\mathbf{r})$, correlation value map $\chi(\mathbf{r}_p, \mathbf{r}_{p'})$ and tSNR map $\text{tSNR}(\mathbf{r})$ defined according to:

¹If necessary the action of the affine transformation operator upon an image can be explicitly written as $\mathcal{A}\rho(\mathbf{r}) = \rho(\mathbf{R}\mathbf{r} - \mathbf{r}_o)$ where \mathbf{R} , a matrix representing rotation about the object's center of mass, and \mathbf{r}_o , a vector representing translation of the center of mass, are functions of t_n .

²If need be, the inverse affine transformation can be written more explicitly as $\mathcal{A}^{-1}\rho(\mathbf{r}) = \rho(\mathbf{R}^{-1}(\mathbf{r} - \mathbf{r}_o))$.

$$D_p(\mathbf{r}) = \frac{|\hat{\rho}_c(\mathbf{r}, t_2) - \hat{\rho}_c(\mathbf{r}, t_1)|}{\hat{\rho}_c(\mathbf{r}, t_1)} \times 100 \quad (7)$$

$$\chi(\mathbf{r}_p, \mathbf{r}_{p'}) = \frac{E[(\hat{\rho}_c(\mathbf{r}_p, t_n) - \mu_{\mathbf{r}_p})(\hat{\rho}_c(\mathbf{r}_{p'}, t_n) - \mu_{\mathbf{r}_{p'}})]}{\sigma_{\mathbf{r}_p} \sigma_{\mathbf{r}_{p'}}} \quad (8)$$

$$\text{tSNR}(\mathbf{r}) = \frac{E[\hat{\rho}_c(\mathbf{r}, t_n)]}{\sqrt{E[|\hat{\rho}_c(\mathbf{r}, t_n)|^2] - |E[\hat{\rho}_c(\mathbf{r}, t_n)]|^2}} \quad (9)$$

where E denotes the expectation value with respect to time t_n while $\mu_{\mathbf{r}}$ and $\sigma_{\mathbf{r}}$ are respectively the mean and standard deviations of the simulated $\hat{\rho}_c(\mathbf{r}, t_n)$.

When calculating the percent difference and the correlation map for our simulations we will neglect the noise term η_m . This results in the following quantities which are independent of the imaged object $\rho(\mathbf{r})$:

$$D_p(\mathbf{r}) = \frac{|C(\mathbf{r}, t_2) - C(\mathbf{r}, t_1)|}{C(\mathbf{r}, t_1)} \times 100 \quad (10)$$

$$\chi(\mathbf{r}_p, \mathbf{r}_{p'}) = \frac{E[(C(\mathbf{r}_p, t_n) - \mu_{\mathbf{r}_p})(C(\mathbf{r}_{p'}, t_n) - \mu_{\mathbf{r}_{p'}})]}{\sqrt{E[(C(\mathbf{r}_p, t_n) - \mu_{\mathbf{r}_p})^2]} \sqrt{E[(C(\mathbf{r}_{p'}, t_n) - \mu_{\mathbf{r}_{p'}})^2]}} \quad (11)$$

where the net receive field contrast $C(\mathbf{r}, t_n)$ is given by

$$C(\mathbf{r}, t_n) = \left(\sum_{m=1}^M |\mathcal{A}^{-1}(t_n) c_m(\mathbf{r})|^2 \right)^{1/2}. \quad (12)$$

When calculating the simulated tSNR we will assume that the image is uniform, $\rho(\mathbf{r}) = 1$, so that we may isolate the RFC-MoCo effect from brain contrast effects. In this case we may then write

$$\text{tSNR}(\mathbf{r}) = \frac{E \left[\left(\sum_{m=1}^M |\mathcal{A}^{-1}(t_n) c_m(\mathbf{r}) + \eta_m|^2 \right)^{1/2} \right]}{\sqrt{E \left[\sum_{m=1}^M |\mathcal{A}^{-1}(t_n) c_m(\mathbf{r}) + \eta_m|^2 \right] - \left| E \left[\sqrt{\sum_{m=1}^M |\mathcal{A}^{-1}(t_n) c_m(\mathbf{r}) + \eta_m|^2} \right] \right|^2}}}. \quad (13)$$

When the motion of the object is a small translation, that is $\mathbf{r}_o(t) = \delta\mathbf{r}(t)$ (see Appendix C) we can approximate Equations (10) and (11) by

$$D_p(\mathbf{r}) = \frac{|[\delta\mathbf{r}(t_2) - \delta\mathbf{r}(t_1)] \cdot \nabla C_{sos}(\mathbf{r}, t_2)|}{C_{sos}(\mathbf{r}, t_1)} \times 100 \quad (14)$$

$$\chi(\mathbf{r}_p, \mathbf{r}_{p'}) = \frac{E[(\delta\mathbf{r}(t_n) \cdot \nabla C_{sos}(\mathbf{r}_p, 0))(\delta\mathbf{r}(t_n) \cdot \nabla C_{sos}(\mathbf{r}_{p'}, 0))]}{\sqrt{E[(\delta\mathbf{r}(t_n) \cdot \nabla C_{sos}(\mathbf{r}_p, 0))^2]} \sqrt{E[(\delta\mathbf{r}(t_n) \cdot \nabla C_{sos}(\mathbf{r}_{p'}, 0))^2]}}, \quad (15)$$

where in deriving Equation (15) we have assumed that $E[\delta\mathbf{r}(t_n)] = 0$ as will be the case in our simulations.

Although Equations (14) and (15) will not be used in our simulations of the RFC-MoCo effect these equations can be helpful with respect to understanding the effect. For example Equation (14) shows that the percent difference should be directly proportional to the translational displacement and the gradient of the SOS contrast field. Also from Equation (15) it should be clear that if the small translations are in only one direction then the correlation map takes the value 1 or -1 depending upon the sign of $\nabla C_{sos}(\mathbf{r}_p)$ and $\nabla C_{sos}(\mathbf{r}_{p'})$ at the seed and map points respectively. When the motion in each dimension is temporally different then $-1 \leq \chi(\mathbf{r}_p, \mathbf{r}_{p'}) \leq 1$ and the correlation map can have a more interesting structure, as will be seen in the results section of this paper.

3. Methods

In this section we: (1) Describe the calculation of the simulated temporally varying receive field contrast for the 16-leg birdcage and 12-channel array head coils; (2) Describe the calculation of the metrics of the RFC-MoCo effect - percent difference, temporal correlation and tSNR maps - in a representative transverse (orthogonal to the long axis of the head coil) plane at $z = 90$ mm. Each coil has a radius of 130 mm at the plane of interest and the metrics are calculated over a 110 mm radius region centered in this plane. This is equivalent to assuming a simulated spherical phantom having a diameter of 220 mm - comparable to a typical image field-of-view for an adult human head - which is centered within the head coil. A uniform signal intensity from all points in space was assumed, thereby allowing us to investigate the RFC-MoCo effect in the absence of image contrast, transmission field heterogeneity and magnetic susceptibility gradient effects.

3.1. Simulating the Temporally Varying RFC

To calculate the receive fields of the head coils we construct the coil or coil elements as a composite of line segments of current. As shown in Appendix A the receive field due to a single line segment with specified endpoints and current amplitude can be written in an exact mathematical form by means of a Biot-Savart Law integration. Then to translate the receive field at time t_n , thereby creating a time series of simulated RFC-MoCo data, we simply translate each endpoint of the line segments comprising the head coil or coil elements. All calculations were performed using C++ code and since the mathematical form of the receive field is known exactly then all calculations will be exact to within machine precision. Note that for both head coils we will neglect the effects of coil loading and mutual inductance between current-carrying line segments. Although the error due to these approximations is significant in the precise design and operation of receive coils it should not change the results given in this paper significantly.

Some of the simulations will be performed using a time series of realistic translational head motion data. Figure 1 shows this realistic center-of-mass translation as a function of time. This motion data was obtained from the output of the FSL (FMRIB Software Library, University of Oxford, UK.) motion correction algorithm (MCFLIRT) (Jenkinson et al., 2002) for a human subject in an actual fMRI experiment and is representative of motion data obtained on normal adult subjects at 3 T. The temporal mean of the motion was subtracted from the data in accordance with the assumptions of our motion model. To test the effects of variable overall motion the motion data is variably scaled to yield specific amounts of root-mean-square motion.

16-Leg Birdcage Coil

Figure 2 depicts a birdcage coil of the type used in this paper. In mode 1, the most spatially homogeneous mode (Jin, 1989) the time-independent part of the mesh current I_n is given by:

$$I_n = C \cos(2\pi n/N) \quad (16)$$

where N is the number of legs (struts) in the coil and C is a constant which will not be of consequence in this paper. The current \mathcal{I}_n in the n^{th} leg is given by $\mathcal{I}_n = I_n - I_{n-1}$.

The endpoints of line segments comprising the legs and endrings of the birdcage coil are arranged symmetrically on a cylindrical surface of 130 mm radius. Figure 3 shows the receive field for such a birdcage coil. The field is plotted over

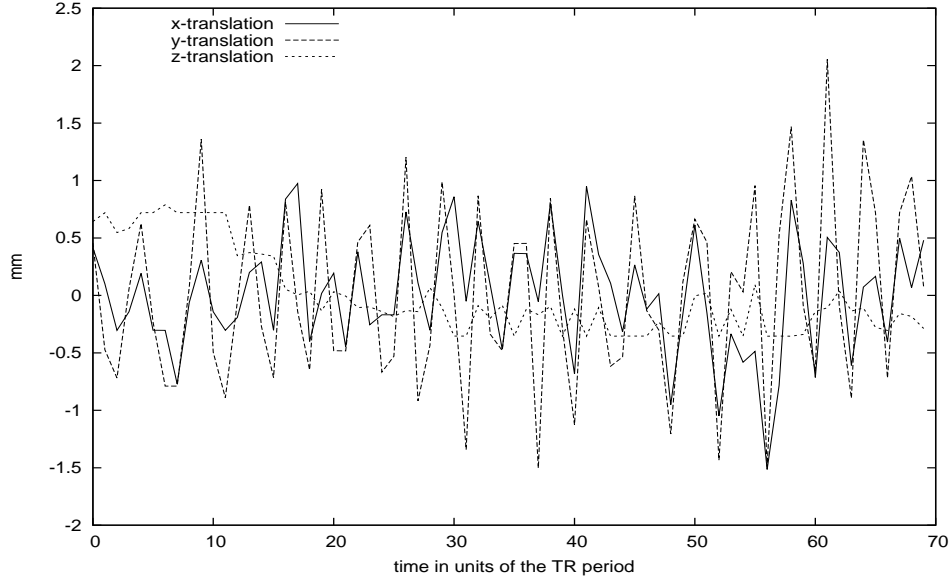


Figure 1: The time series of translational displacements used in the tSNR and correlation value calculations.

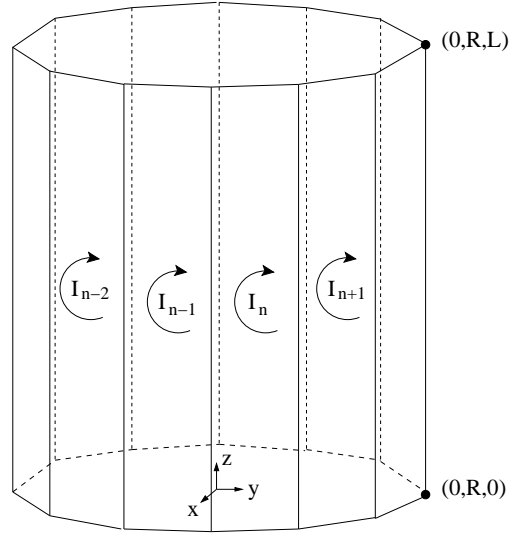


Figure 2: The simulations are done with a 16-leg birdcage coil but here we depict a 12-leg coil to avoid clutter in the figure and clearly convey the general coil geometry. The coil is depicted with mesh currents I_n ($n = 1, \dots, N$) where N is the number of legs. Note that the lower end ring lies in the $z = 0$ mm plane.

an axially-sliced region of a 110 mm radius which is centered transversely within the coil. The important thing to note about Figure 3 is that the birdcage coil gives a receive field which varies by approximately 30% over the region shown.

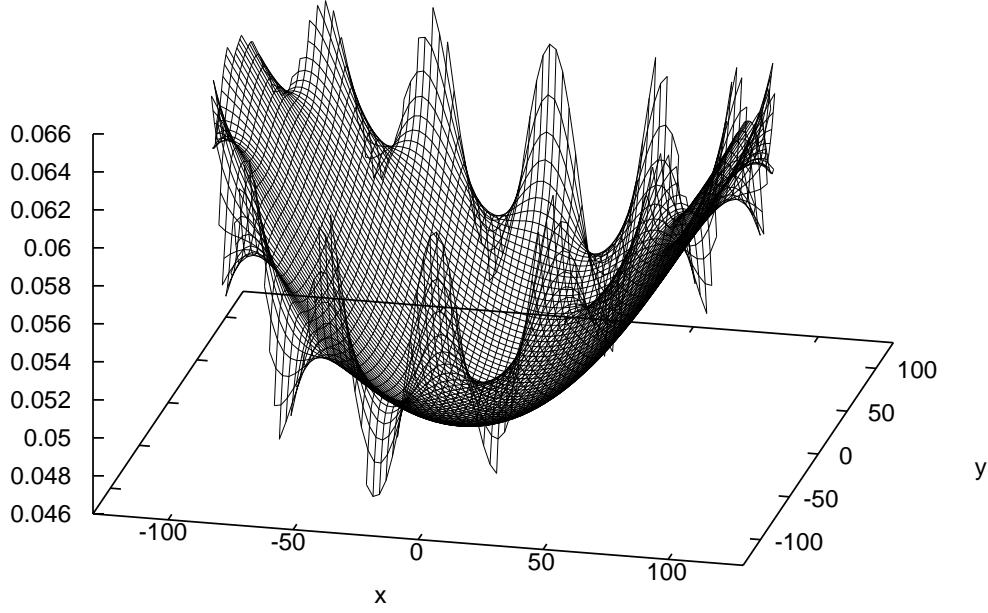


Figure 3: Receive field magnitude for 16-leg birdcage coil geometry (coil radius = 130 mm, coil length $L = 186$ mm). The field is plotted over a region of radius 110 mm centered in the transverse plane at $z = 90$ within the coil. The receive field magnitude is plotted as a unitless quantity since the homogeneity of the field is our primary concern in this paper.

12-Channel Array

The simulated 12-channel array consists of $M = 12$ coil elements of the general form shown in Figure 4 in which the coil element is comprised of six segments each with a unit current in the clockwise direction from the perspective of an observer external to the array. Figure 5 depicts segment 1 of each coil element, which are taken to lie in a single transverse plane (the x,y -plane). The endpoints of the six line segments comprising each coil element lie on a cylindrical surface of 130 mm radius (see Appendix B) and closely approximate the geometry of commercially available head coils. The sum of the fields due to each of the line segments comprising a given coil element yields the receive field of that coil element. The final SOS receive field is then calculated from the receive

fields of the individual coil elements according to Equation (2).

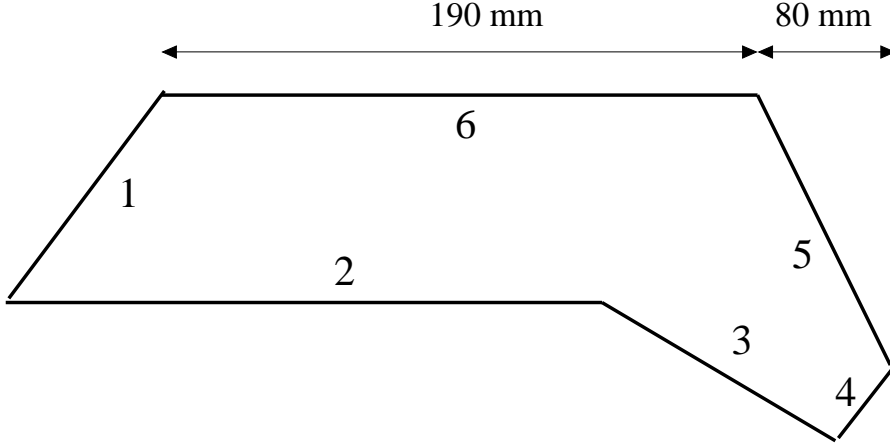


Figure 4: The general shape of a single coil element for the 12-element array coil. The length of segments 2 and 6 are the same for all elements. Segments 1 lie in the $z = 0$ transverse plane.

Figure 6 shows the SOS receive field for the simulated 12-channel array. The field is plotted over an axially-sliced region of 110 mm radius which is centered transversely within the receive array. The important thing to note about Figure 6 is that the 12-channel array gives a receive field which varies by as much as 400% over the region shown.

3.2. Calculating RFC-MoCo Effect Metrics

Percent Difference

For both head coil geometries we estimate the magnitude of the RFC-MoCo effect size by calculating the percent difference map, given by Equation (10), when the object is displaced translationally by 1 mm in the y-direction. For both head coils we also calculate the average and maximum of the percent difference map over the 110 mm radius region when the object is displaced by 0 to 3.5 mm. For the percent difference calculations no noise is added to the simulated data.

Temporal Correlation

We examine potential effects upon temporal correlation maps due to the RFC-MoCo effect for translational head motion in the 12-channel array only. These simulations are performed by using the time series of realistic head motion

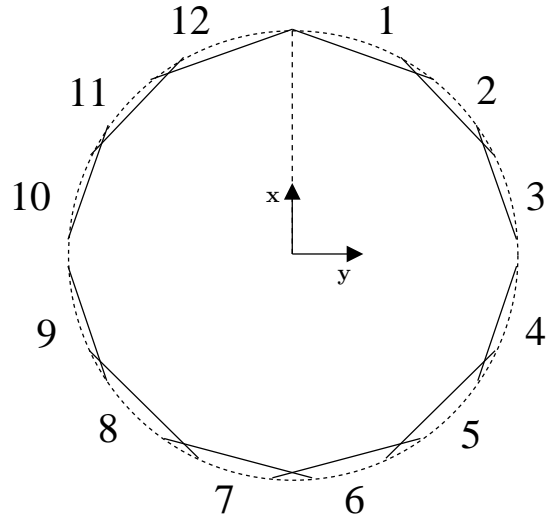


Figure 5: Cross-section of the simulated 12-channel receiver array showing length and orientations for segment 1 of each coil element. The z-axis (parallel to B_0), of a right-handed coordinate system, points into the plane of the page.

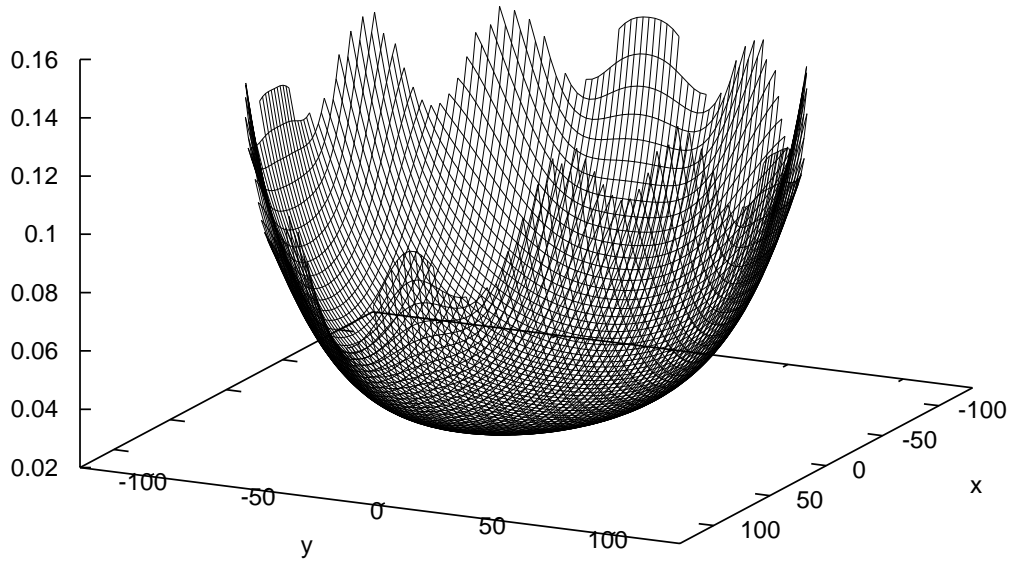


Figure 6: SOS receive field over an axially-sliced region of radius 110 mm which is centered in the transverse plane at $z = 90$ within the 12-element receive array. The receive field magnitude is plotted as a unitless quantity since the homogeneity of the field is our primary concern in this paper.

variables (see Figure 1) and calculating temporal correlation maps according to Equation (11). To calculate the temporal correlation maps we set the root-mean-square (rms) magnitude of the translational motion to 1 mm but it should be noted that for small translations we expect, from Equation (15), that the correlation maps will be independent of the magnitude of the motion. The correlation is between a seed point at $x = -104$ mm, $y = 0$ mm and $z = 90$ mm and all points within the same axially-sliced ($z = 90$ mm) region of radius 110 mm which is centered within the array. For the temporal correlation calculations no noise is added to the simulated data because our principal concern is elucidating the general features one might expect to see in a temporal correlation map when the RFC-MoCo effect is of significant size ³.

tSNR

For the 12-channel array only we investigate the spatial dependence of the tSNR maps for varying amounts of realistic translational head motion (see Figure 1) and spatially uniform Gaussian electronic noise η_m . The noise is applied to the complex-valued time series image data according to Equation (13) such that it yields a tSNR level, 80 at the center of the image, representative of the tSNR seen in a 3-minute $T2^*$ -weighted EPI time series at 3 T. TSNR maps were obtained for rms motion values of 0.0, 0.5, 1.0 and 2.5 mm.

4. Results

Percent Difference

Figures 7 and 8 show the percent difference in the receive field contrast due to a 1 mm translation in the y-direction for the 16-leg birdcage and 12-channel array head coils, respectively. From these figures it should be clear that this particular birdcage coil geometry yields significant reduction in the RFC-MoCo effect as compared to the 12-channel array. It is also clear that the RFC-MoCo effect for the 12-channel array is of similar magnitude if not greater than the percent difference expected from the BOLD effect at most points in this axial slice. Hence the effect should be an important systematic error in fMRI analysis if an array coil is used as the receiver.

Figure 9 shows a plot of the average percent difference and the maximum percent difference over the 110 mm radius region of an axial slice at $z = 90$ mm versus the displacement in the y-direction. The trend is approximately linear, as would be expected for small displacements (see Equation (C.4)).

³The significance is established by the percent difference maps

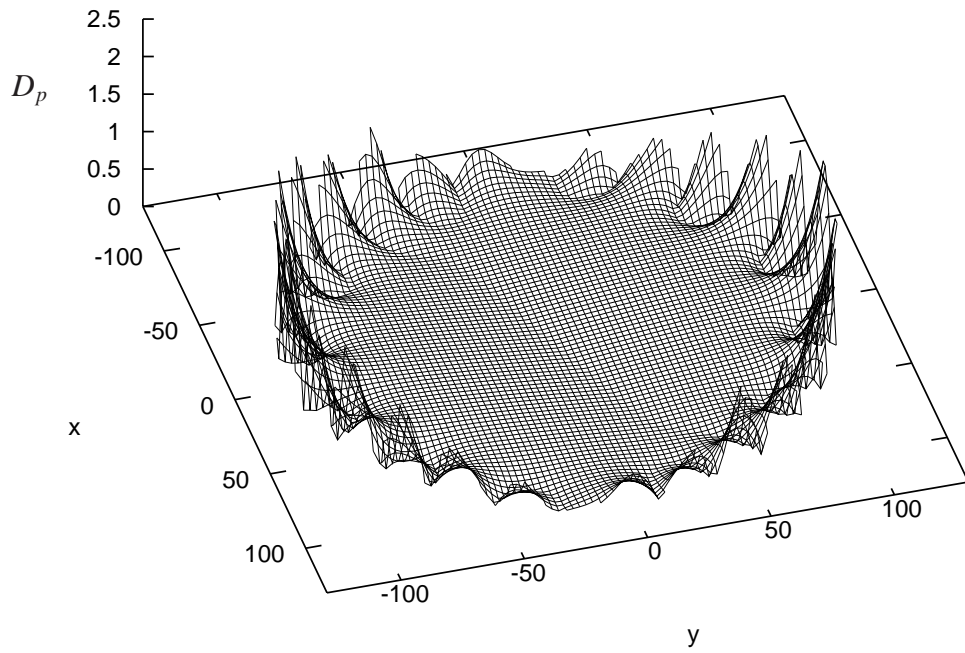


Figure 7: Percent difference in receive field contrast due to 1 mm motion in the y-direction for the 16-leg birdcage receive coil geometry (radius = 130 mm). The percent difference is plotted over an axially-sliced region of radius = 110 mm which is centered within the array.

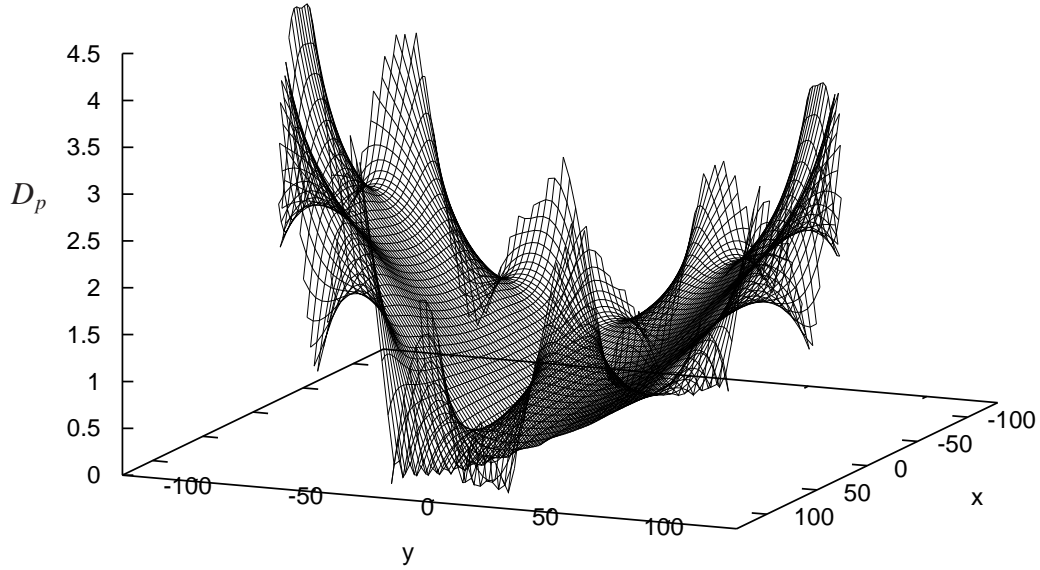


Figure 8: Percent difference in receive field contrast due to 1 mm motion in the y-direction for the 12-channel receiver array geometry (radius = 130 mm). The percent difference is plotted over an axially-sliced region of radius = 110 mm which is centered within the array.

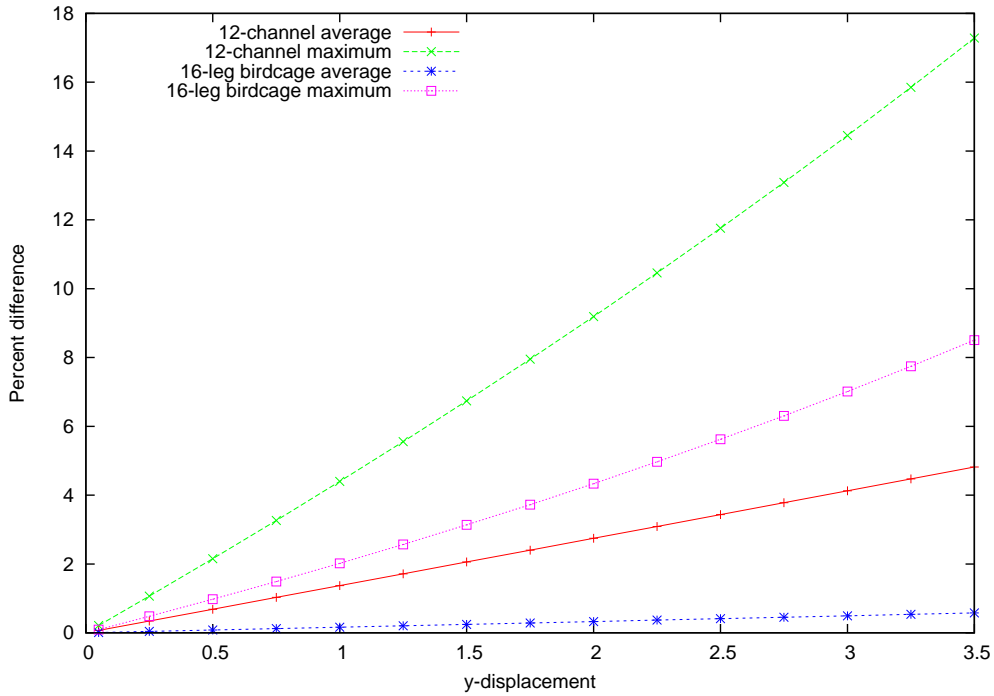


Figure 9: Comparison of percent difference between 16-leg birdcage and 12-channel array receiver head coils. Average and maximum percent difference over an axially-sliced region of radius = 110 mm which is centered within each coil are plotted versus displacement in the y-direction.

Temporal Correlation

Figure 10 is a surface plot showing the temporal correlation value as a function of location within an axial slice. The correlation is between a seed point at $x = -104$ mm, $y = 0$ mm and $z = 90$ mm and all points within the same axially-sliced ($z = 90$ mm) region of radius 110 mm which is centered within the array. For reference the value of χ at the seed point (1.0 as expected) is indicated by a red dot on the 3D surface. Notice the negative as well as positive correlation values.

tSNR

Figures 11 through 14 show the tSNR surface plots for the cases of no motion, 0.5 mm, 1.0 mm and 2.5 mm rms motion for the 12-channel receive array. Color and viewpoint is different for each surface plot to aid in the visualization of the surface. Please refer to the axes for quantitative information. At 0.5 mm rms motion (Figure 12) much of the tSNR benefit from the multiple channels is eliminated through the RFC-MoCo effect. At 1.0 mm rms motion (Figure 13) the flattening of the tSNR map is effectively complete. At 2.5 mm rms motion (Figure 14), which approximately corresponds to a pixel shift for the chosen

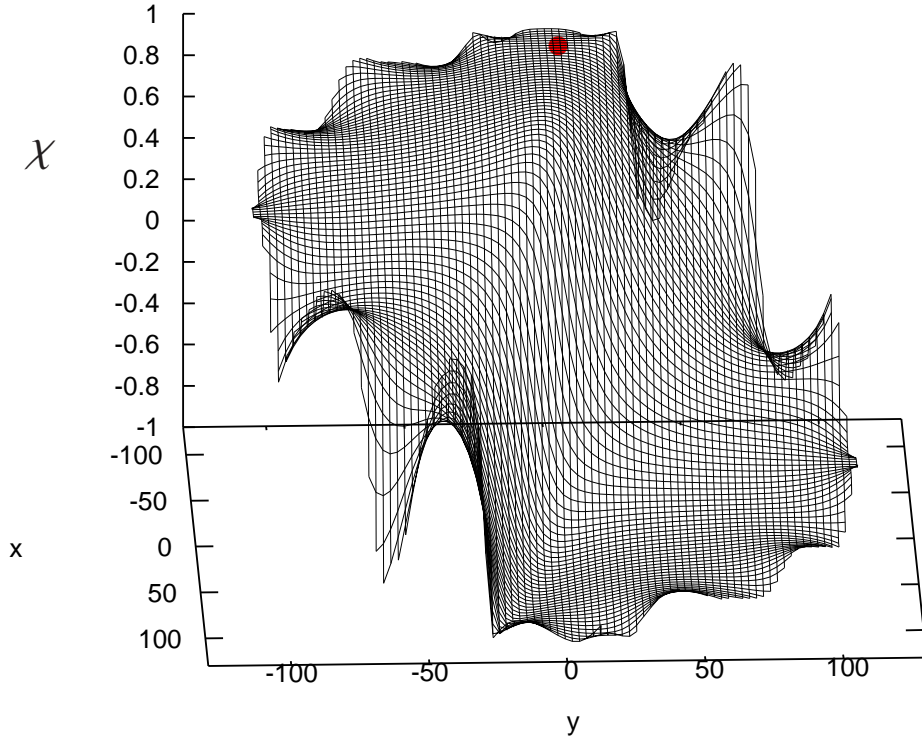


Figure 10: A surface plot showing the temporal correlation value $\chi(\mathbf{r}_p, \mathbf{r}_{p'})$ as a function position within an axial slice. The correlation is between a seed point $\mathbf{r}_{p'}$ at $x = -104$ mm, $y = 0$ mm and $z = 90$ mm and all points \mathbf{r}_p within the same axially-sliced ($z = 90$ mm) region of radius $= 110$ mm which is centered within the array. For reference the value of χ at the seed point is indicated by a red dot. The motion was purely translational (1 mm rms) and taken from the output of the FSL (FMRIB's Software Library) MCFLIRT motion correction code (see Figure 1).

electronic noise tSNR, the tSNR in regions nearest the coils is much reduced compared to that at the center of the array. Degradation of tSNR would be expected for all brain regions.

5. Discussion

We set out to assess how receive field contrast could possibly limit the fidelity of motion-corrected time series MRI measurements acquired in the presence of significant subject motion. Simulations were performed so that the specific interaction of the receive field contrast and motion could be assessed without the complicating factors, such as head-fixed image contrast and imperfect motion correction, that would likely arise in experimental data.

We have shown in this work that: (1) The RFC-MoCo effect should be expected to compete with the BOLD effect for a typical 12-channel cylindrical array, (2) Interesting temporal correlations occur as a result of the RFC-MoCo effect that will compete with the temporal correlations due to the BOLD effect and (3) Moderate amounts of motion lead to serious tSNR degradation in regions of the 12-channel array receive field where, from consideration of the

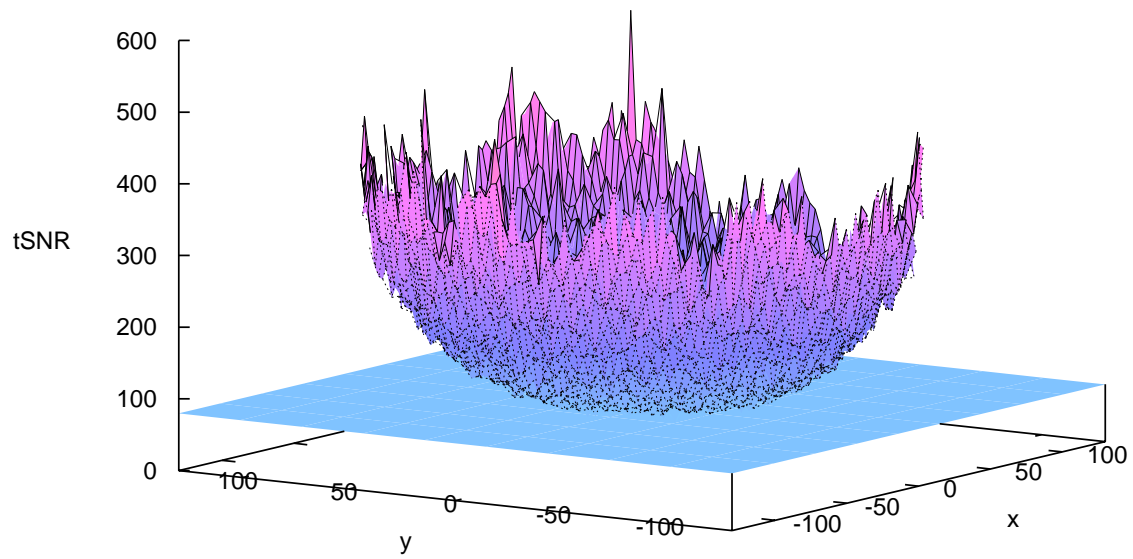


Figure 11: A surface plot showing the tSNR for the case of no motion as a function of location within an axially-sliced ($z = 90$ mm) region of radius = 110 mm which is centered within the 12-element array. The tSNR is 80 at the center of this region.

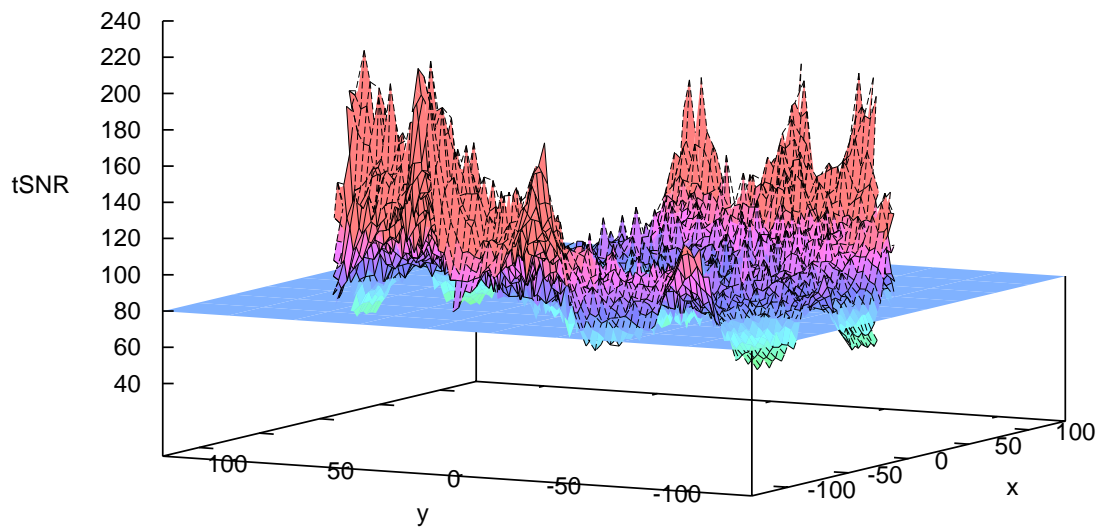


Figure 12: A surface plot showing the tSNR for the case of 0.5 mm rms motion as a function of location within an axially-sliced ($z = 90$ mm) region of radius = 110 mm which is centered within the 12-element array. The motion was purely translational and taken from the output of the FSL (FMRIB's Software Library) MCFLIRT motion correction code.

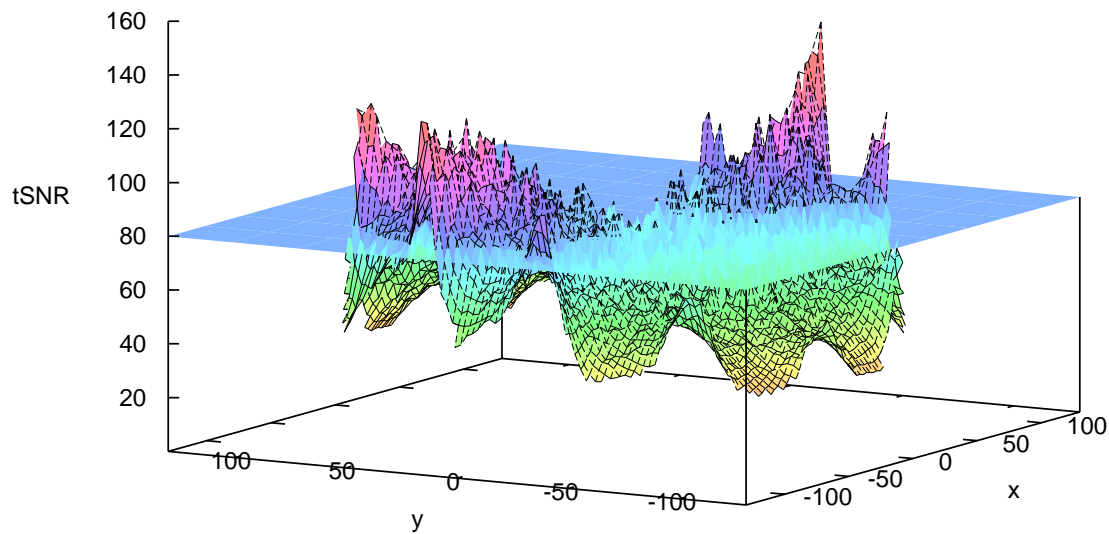


Figure 13: A surface plot showing the tSNR for the case of 1.0 mm rms motion as a function of location within an axially-sliced ($z = 90$ mm) region of radius = 110 mm which is centered within the 12-element array. The motion was purely translational and taken from the output of the FSL (FMRIB's Software Library) MCFLIRT motion correction code.

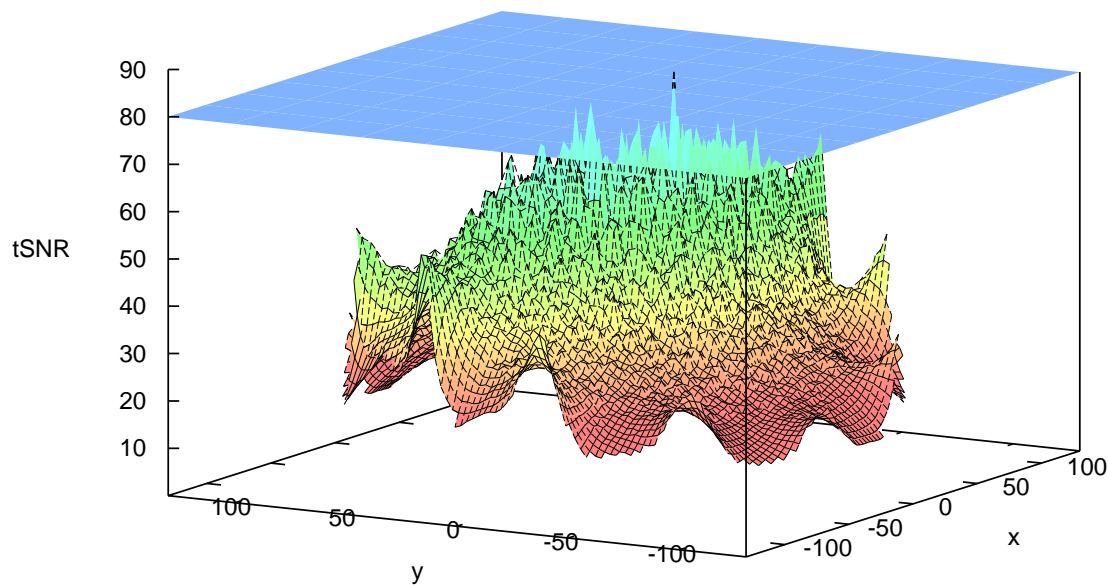


Figure 14: A surface plot showing the tSNR for the case of 2.5 mm (the size of a pixel typically associated with the tSNR at the center of the array) rms motion as a function of location within an axially-sliced ($z = 90$ mm) region of radius = 110 mm which is centered within the 12-element array. The motion was purely translational and taken from the output of the FSL (FMRIB's Software Library) MCFLIRT motion correction code.

signal magnitude alone, one might expect improved tSNR.

Caution should be exercised in interpreting the results given here for several reasons:

1. The effects of mutual inductance and coil loading were both neglected. We do not expect the neglect of these two complicating effects to do anything but create greater local variability of the receive array SOS pattern and hence even greater RFC-MoCo effect.
2. We have assumed the current-carrying conductors of the simulated head coils to be thin wires. The conductors of real head coils are thin tracings with a width (parallel to the cylindrical surface of the head coil) in the neighborhood of 3 mm. The width of the real conductors should have a spatially smoothing effect which would be expected to reduce the RFC-MoCo effect to some extent.
3. We used a root-sum-of-squares reconstruction of the final image. While this method of reconstructing images from coil arrays is ubiquitous, other image combination methods are available such as the adaptive combination of coil images (Walsh et al., 2000), and these methods should perform differently with respect to the specific results of RFC-MoCo.
4. We have not simulated rotational motion of the head in this work and the presence of rotation should be expected to give even more interesting correlation maps.
5. Some manufactures combine the receive fields from the 12 coil elements in various manners to produce arrays that may be effectively smaller (eg. the "CP" and "Dual" receive modes of Siemens 3T Trio scanners) with correspondingly more homogeneous receive fields. These coil combination approaches should establish reduced RFC-MoCo effects compared to the full multi-element array operation, but the remaining RFC-MoCo effect is likely to be larger than for a birdcage coil having similar physical dimensions.

In a real fMRI experiment our assumption of perfect motion correction will not be satisfied and the degree to which the RFC-MoCo effect will influence the time series data will depend upon the accuracy of the applied motion correction algorithm. When imperfect motion correction is applied there will be a mixing of the various contrasts present in the image - those fixed relative to the head and those fixed relative to the scanner. Furthermore, the presence of receive field contrast, as with other contrasts that are fixed relative to the scanner, is expected to degrade motion correction performance through an underestimate of

the actual motion - an effect we term the "anchoring effect." We are investigating the magnitude of the RFC-anchoring effect in parallel work. (Other scanner-fixed contrast mechanisms will generate their own anchoring effects.)

The question naturally arises as to the practical relevance of the results presented here for the RFC-MoCo effect. In the first instance, the 12-channel array was simulated in a manner that may not be appropriate for some scanner vendors. For example, in the absence of acceleration the default coil reception mode on a Siemens scanner would be "CP mode" (Reykowski, 2006) which is designed to provide near optimum SNR in the center region of the image. Thus, we cannot yet give a clear ranking of the RFC-MoCo effect's contribution to spurious correlations due to all causes in resting-state fMRI studies. We will attempt to clarify this ranking in future simulation work.

Data processing methods such as independent component analysis (Kundu et al., 2012) may be able to discriminate between artifactual and neurally-driven correlations in some circumstances, but it has not yet been established that the motion metrics output from the commonly used affine correction algorithms will capture sufficiently all the correlations introduced by the RFC-MoCo effect. Recent work by Power et al. (Power et al., 2011) suggests that some spurious correlations can be disambiguated by removing networks correlated with motion parameters, but further work is needed to establish the efficacy of this approach.

In follow up simulations we will provide a similar analysis to that presented in this work for the CP, dual, triple modes of the 12-channel head array. We will also present a similar analysis for a 32-channel array which has smaller somewhat hexagonally shaped coil elements arranged on the surface of a roughly spherical shell. Compared to the results given in this work we would expect the RFC-MoCo effect to be larger for the 32-channel array and smaller for dual and CP modes of the 12-channel array. We will then be in a better position to make quantitative estimates of the severity of the RFC-MoCo issue for connectivity studies from resting state data, and to compare the relative performance of 32-channel and 12-channel array coils for time series EPI under motion limiting regimes.

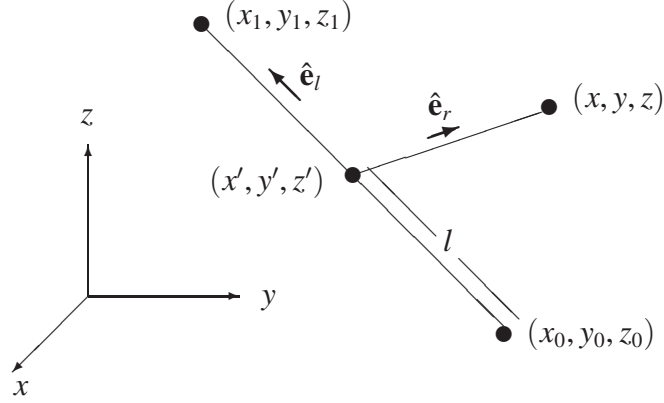


Figure A.15: A line element specified by the endpoints (x_0, y_0, z_0) and (x_1, y_1, z_1) and carrying a unit current in the direction of the unit vector $\hat{\mathbf{e}}_l$. The receive field is to be calculated at points (x, y, z) .

Appendix A. Magnetic Field Due To An Arbitrarily Oriented Current Carrying Line Segment

In this section we derive the receive field due to a single line element. This result will be used to calculate the receive field of a coil element that can be constructed from a set of such line elements. Figure A.15 depicts one such line element.

The magnetic field \mathbf{B} due to the line element can be calculated from the following form of the Biot-Savart Law:

$$\mathbf{B} = \int_0^L \frac{\hat{\mathbf{e}}_l \times \hat{\mathbf{e}}_r}{r^2} dl. \quad (\text{A.1})$$

The unit vectors $\hat{\mathbf{e}}_l$ and $\hat{\mathbf{e}}_r$ are given by

$$\hat{\mathbf{e}}_l = \frac{\Delta x}{L} \hat{\mathbf{x}} + \frac{\Delta y}{L} \hat{\mathbf{y}} + \frac{\Delta z}{L} \hat{\mathbf{z}} \quad (\text{A.2})$$

where $\Delta x = x_1 - x_0$ etc and

$$\hat{\mathbf{e}}_r = \frac{x - x'}{r} \hat{\mathbf{x}} + \frac{y - y'}{r} \hat{\mathbf{y}} + \frac{z - z'}{r} \hat{\mathbf{z}} \quad (\text{A.3})$$

where

$$L = \sqrt{(\Delta x)^2 + (\Delta y)^2 + (\Delta z)^2} \quad (\text{A.4})$$

and

$$r = \sqrt{(x - x')^2 + (y - y')^2 + (z - z')^2}. \quad (\text{A.5})$$

Since

$$x' = x_0 + l\hat{\mathbf{e}}_l \cdot \hat{\mathbf{x}} = x_0 + (l/L)\Delta x \quad (\text{A.6})$$

$$y' = y_0 + l\hat{\mathbf{e}}_l \cdot \hat{\mathbf{y}} = y_0 + (l/L)\Delta y \quad (\text{A.7})$$

$$z' = z_0 + l\hat{\mathbf{e}}_l \cdot \hat{\mathbf{z}} = z_0 + (l/L)\Delta z \quad (\text{A.8})$$

then

$$\hat{\mathbf{e}}_r = r^{-1}[x - x_0 - (l/L)\Delta x] \hat{\mathbf{x}} \quad (\text{A.9})$$

$$+ r^{-1}[y - y_0 - (l/L)\Delta y] \hat{\mathbf{y}} \quad (\text{A.10})$$

$$+ r^{-1}[z - z_0 - (l/L)\Delta z] \hat{\mathbf{z}} \quad (\text{A.11})$$

and

$$r = \sqrt{[x - x_0 - l\Delta x/L]^2 + [y - y_0 - l\Delta y/L]^2 + [z - z_0 - l\Delta z/L]^2}. \quad (\text{A.12})$$

Since

$$\hat{\mathbf{e}}_l \times \hat{\mathbf{e}}_r = \begin{vmatrix} \hat{\mathbf{x}} & \hat{\mathbf{y}} & \hat{\mathbf{z}} \\ \frac{x_1 - x_0}{L} & \frac{y_1 - y_0}{L} & \frac{z_1 - z_0}{L} \\ \frac{x - x'}{r} & \frac{y - y'}{r} & \frac{z - z'}{r} \end{vmatrix} \quad (\text{A.13})$$

$$\begin{aligned} &= (Lr)^{-1}[\Delta y(z - z') - \Delta z(y - y')] \hat{\mathbf{x}} \\ &+ (Lr)^{-1}[\Delta z(x - x') - \Delta x(z - z')] \hat{\mathbf{y}} \\ &+ (Lr)^{-1}[\Delta x(y - y') - \Delta y(x - x')] \hat{\mathbf{z}} \end{aligned} \quad (\text{A.14})$$

$$\begin{aligned} &= (Lr)^{-1}[\Delta y(z - z_0 - l\Delta z/L) - \Delta z(y - y_0 - l\Delta y/L)] \hat{\mathbf{x}} \\ &+ (Lr)^{-1}[\Delta z(x - x_0 - l\Delta x/L) - \Delta x(z - z_0 - l\Delta z/L)] \hat{\mathbf{y}} \\ &+ (Lr)^{-1}[\Delta x(y - y_0 - l\Delta y/L) - \Delta y(x - x_0 - l\Delta x/L)] \hat{\mathbf{z}} \end{aligned} \quad (\text{A.15})$$

then

$$B_x(x, y, z) = \frac{\Delta y}{L} \int_0^L \frac{z - z_0 - l\Delta z/L}{r^3} dl - \frac{\Delta z}{L} \int_0^L \frac{y - y_0 - l\Delta y/L}{r^3} dl \quad (\text{A.16})$$

$$B_y(x, y, z) = \frac{\Delta z}{L} \int_0^L \frac{x - x_0 - l\Delta x/L}{r^3} dl - \frac{\Delta x}{L} \int_0^L \frac{z - z_0 - l\Delta z/L}{r^3} dl \quad (\text{A.17})$$

$$B_z(x, y, z) = \frac{\Delta x}{L} \int_0^L \frac{y - y_0 - l\Delta y/L}{r^3} dl - \frac{\Delta y}{L} \int_0^L \frac{x - x_0 - l\Delta x/L}{r^3} dl \quad (\text{A.18})$$

where

$$\begin{aligned}
r^2 &= (x - x_0)^2 - 2(l/L)\Delta x(x - x_0) + (l/L)^2(\Delta x)^2 \\
&+ (y - y_0)^2 - 2(l/L)\Delta y(y - y_0) + (l/L)^2(\Delta y)^2 \\
&+ (z - z_0)^2 - 2(l/L)\Delta z(z - z_0) + (l/L)^2(\Delta z)^2
\end{aligned} \tag{A.19}$$

$$\begin{aligned}
&= (x - x_0)^2 + (y - y_0)^2 + (z - z_0)^2 \\
&- 2(l/L)[(x - x_0)\Delta x + (y - y_0)\Delta y + (z - z_0)\Delta z] + l^2.
\end{aligned} \tag{A.20}$$

Substituting

$$B_x(x, y, z) = \frac{\Delta y}{L} \int_0^L \frac{z - z_0 - l\Delta z/L}{[l^2 - \beta l + \kappa]^{3/2}} dl - \frac{\Delta z}{L} \int_0^L \frac{y - y_0 - l\Delta y/L}{[l^2 - \beta l + \kappa]^{3/2}} dl \tag{A.21}$$

$$B_y(x, y, z) = \frac{\Delta z}{L} \int_0^L \frac{x - x_0 - l\Delta x/L}{[l^2 - \beta l + \kappa]^{3/2}} dl - \frac{\Delta x}{L} \int_0^L \frac{z - z_0 - l\Delta z/L}{[l^2 - \beta l + \kappa]^{3/2}} dl \tag{A.22}$$

$$B_z(x, y, z) = \frac{\Delta x}{L} \int_0^L \frac{y - y_0 - l\Delta y/L}{[l^2 - \beta l + \kappa]^{3/2}} dl - \frac{\Delta y}{L} \int_0^L \frac{x - x_0 - l\Delta x/L}{[l^2 - \beta l + \kappa]^{3/2}} dl \tag{A.23}$$

where

$$\kappa = (x - x_0)^2 + (y - y_0)^2 + (z - z_0)^2 \tag{A.24}$$

$$\beta = (2/L)[(x - x_0)\Delta x + (y - y_0)\Delta y + (z - z_0)\Delta z]. \tag{A.25}$$

From the integral tables

$$\int \frac{d + ex}{[ax^2 + bx + c]^{3/2}} dx = \frac{2bd - 4ce + (4ad - 2be)x}{(4ac - b^2)(ax^2 + bx + c)^{1/2}} \tag{A.26}$$

so that

$$\begin{aligned}
\int_0^L \frac{d + ex}{[x^2 + bx + c]^{3/2}} dx &= \frac{2bd - 4ce + (4d - 2be)L}{(4c - b^2)(L^2 + bL + c)^{1/2}} + \frac{4ce - 2bd}{c^{1/2}(4c - b^2)} \\
&= \frac{(4L + 2b)d - (4c + 2bL)e}{(4c - b^2)(L^2 + bL + c)^{1/2}} + \frac{4ce - 2bd}{c^{1/2}(4c - b^2)}.
\end{aligned} \tag{A.27}$$

We can then write

$$\begin{aligned}
B_x &= \frac{\Delta y}{L} \left[\frac{(4L - 2\beta)(z - z_0) + (4\kappa - 2\beta L)\Delta z/L}{(4\kappa - \beta^2)(L^2 - \beta L + \kappa)^{1/2}} + \frac{2\beta(z - z_0) - 4\kappa\Delta z/L}{\sqrt{\kappa}(4\kappa - \beta^2)} \right] \\
&- \frac{\Delta z}{L} \left[\frac{(4L - 2\beta)(y - y_0) + (4\kappa - 2\beta L)\Delta y/L}{(4\kappa - \beta^2)(L^2 - \beta L + \kappa)^{1/2}} + \frac{2\beta(y - y_0) - 4\kappa\Delta y/L}{\sqrt{\kappa}(4\kappa - \beta^2)} \right] \\
&= \frac{(4L - 2\beta)[\Delta y(z - z_0) - \Delta z(y - y_0)]}{L(4\kappa - \beta^2)(L^2 - \beta L + \kappa)^{1/2}} \\
&+ \frac{2\beta[\Delta y(z - z_0) - \Delta z(y - y_0)]}{L\sqrt{\kappa}(4\kappa - \beta^2)} \tag{A.28}
\end{aligned}$$

or

$$B_x = \left[\frac{4L - 2\beta}{(L^2 - \beta L + \kappa)^{1/2}} + \frac{2\beta}{\sqrt{\kappa}} \right] \frac{\Delta y(z - z_0) - \Delta z(y - y_0)}{L(4\kappa - \beta^2)}. \tag{A.29}$$

Similarly

$$B_y = \left[\frac{4L - 2\beta}{(L^2 - \beta L + \kappa)^{1/2}} + \frac{2\beta}{\sqrt{\kappa}} \right] \frac{\Delta z(x - x_0) - \Delta x(z - z_0)}{L(4\kappa - \beta^2)} \tag{A.30}$$

and

$$B_z = \left[\frac{4L - 2\beta}{(L^2 - \beta L + \kappa)^{1/2}} + \frac{2\beta}{\sqrt{\kappa}} \right] \frac{\Delta x(y - y_0) - \Delta y(x - x_0)}{L(4\kappa - \beta^2)}. \tag{A.31}$$

Note, as a consistency check, that Equations (A.28), (A.30) and (A.31) reduce to the field due to an infinite length wire with unit current oriented along any of the axes (Arfken, 1985). The receive field for a single line segment wire with unit current directed from point (x_0, y_0, z_0) to point (x_1, y_1, z_1) is then

$$B_r^* = B_x - iB_y \tag{A.32}$$

$$\begin{aligned}
&= \frac{(4L - 2\beta)[\Delta y(z - z_0) - \Delta z(y - y_0)]}{L(4\kappa - \beta^2)(L^2 - \beta L + \kappa)^{1/2}} \\
&+ \frac{2\beta[\Delta y(z - z_0) - \Delta z(y - y_0)]}{L\sqrt{\kappa}(4\kappa - \beta^2)} \\
&- i \frac{(4L - 2\beta)[\Delta z(x - x_0) - \Delta x(z - z_0)]}{L(4\kappa - \beta^2)(L^2 - \beta L + \kappa)^{1/2}} \\
&- i \frac{2\beta[\Delta z(x - x_0) - \Delta x(z - z_0)]}{L\sqrt{\kappa}(4\kappa - \beta^2)}. \tag{A.33}
\end{aligned}$$

Appendix B. 12-Channel Array Geometry

The first end point (x_{nm}^0, y_{nm}^0) and the second end point (x_{nm}^1, y_{nm}^1) of m^{th} segment of the n^{th} coil element are:

Top half of array

$$\begin{aligned}
 x_{11}^0 &= r & y_{11}^0 &= 0 \\
 x_{11}^1 &= r \cos \phi_1 & y_{11}^1 &= r \sin \phi_1 \\
 x_{21}^0 &= r \cos(\phi_1 - \theta_2) & y_{21}^0 &= r \sin(\phi_1 - \theta_2) \\
 x_{21}^1 &= r \cos(\phi_2 + \phi_1 - \theta_2) & y_{21}^1 &= r \sin(\phi_2 + \phi_1 - \theta_2) \\
 x_{31}^0 &= r \cos(\phi_2 + \phi_1 - \theta_2 - \theta_1) & y_{31}^0 &= r \sin(\phi_2 + \phi_1 - \theta_2 - \theta_1) \\
 x_{31}^1 &= r \cos(\phi_3 + \phi_2 + \phi_1 - \theta_2 - \theta_1) & y_{31}^1 &= r \sin(\phi_3 + \phi_2 + \phi_1 - \theta_2 - \theta_1) \\
 x_{12,1}^0 &= r \cos \phi_1 & y_{12,1}^0 &= -r \sin \phi_1 \\
 x_{12,1}^1 &= r & y_{12,1}^1 &= 0 \\
 x_{11,1}^0 &= r \cos(\phi_2 + \phi_1 - \theta_2) & y_{11,1}^0 &= -r \sin(\phi_2 + \phi_1 - \theta_2) \\
 x_{11,1}^1 &= r \cos(\phi_1 - \theta_2) & y_{11,1}^1 &= -r \sin(\phi_1 - \theta_2) \\
 x_{10,1}^0 &= r \cos(\phi_3 + \phi_2 + \phi_1 - \theta_2 - \theta_1) & y_{10,1}^0 &= -r \sin(\phi_3 + \phi_2 + \phi_1 - \theta_2 - \theta_1) \\
 x_{10,1}^1 &= r \cos(\phi_2 + \phi_1 - \theta_2 - \theta_1) & y_{10,1}^1 &= -r \sin(\phi_2 + \phi_1 - \theta_2 - \theta_1)
 \end{aligned}$$

where $\phi_n = 2 \sin^{-1}(l_n/2r)$ is the angle subtended by a chord of length l_n giving the length of segment 1 of the n^{th} coil element and $\theta_n = 2 \sin^{-1}(d_n/2r)$ is the angle subtended by a chord of length d_n giving the chord length of the coil overlap and gaps.

Bottom half of array

$$\begin{aligned}
 x_{41}^0 &= -r \sin \theta_0 & y_{41}^0 &= r \cos \theta_0 \\
 x_{41}^1 &= -r \sin(\phi_4 + \theta_0) & y_{41}^1 &= r \cos(\phi_4 + \theta_0) \\
 x_{51}^0 &= -r \sin(\phi_4 + \theta_0 - \theta_1) & y_{51}^0 &= r \cos(\phi_4 + \theta_0 - \theta_1) \\
 x_{51}^1 &= -r \sin(\phi + \phi_4 + \theta_0 - \theta_1) & y_{51}^1 &= r \cos(\phi + \phi_4 + \theta_0 - \theta_1) \\
 x_{61}^0 &= -r \sin(\phi + \phi_4 + \theta_0 - \theta_1 - \theta_2) & y_{61}^0 &= r \cos(\phi + \phi_4 + \theta_0 - \theta_1 - \theta_2) \\
 x_{61}^1 &= -r \sin(2\phi + \phi_4 + \theta_0 - \theta_1 - \theta_2) & y_{61}^1 &= r \cos(2\phi + \phi_4 + \theta_0 - \theta_1 - \theta_2) \\
 x_{71}^0 &= -r \sin(2\phi + \phi_4 + \theta_0 - \theta_1 - 2\theta_2) & y_{71}^0 &= r \cos(2\phi + \phi_4 + \theta_0 - \theta_1 - 2\theta_2) \\
 x_{71}^1 &= -r \sin(3\phi + \phi_4 + \theta_0 - \theta_1 - 2\theta_2) & y_{71}^1 &= r \cos(3\phi + \phi_4 + \theta_0 - \theta_1 - 2\theta_2) \\
 x_{81}^0 &= -r \sin(3\phi + \phi_4 + \theta_0 - \theta_1 - 3\theta_2) & y_{81}^0 &= r \cos(3\phi + \phi_4 + \theta_0 - \theta_1 - 3\theta_2) \\
 x_{81}^1 &= -r \sin(4\phi + \phi_4 + \theta_0 - \theta_1 - 3\theta_2) & y_{81}^1 &= r \cos(4\phi + \phi_4 + \theta_0 - \theta_1 - 3\theta_2) \\
 x_{91}^0 &= -r \sin(4\phi + \phi_4 + \theta_0 - 2\theta_1 - 3\theta_2) & y_{91}^0 &= r \cos(4\phi + \phi_4 + \theta_0 - 2\theta_1 - 3\theta_2) \\
 x_{91}^1 &= -r \sin \theta_0 & y_{91}^1 &= -r \cos \theta_0
 \end{aligned}$$

where ϕ , the angle subtended by segment 1 for coils 5 through 8, is determined by

the condition $\pi - 2(\phi_4 + \theta_0 - \theta_1) = 4\phi - 3\theta_2$ or $\phi = \pi/4 - (\phi_4 + \theta_0 - \theta_1)/2 + 3\theta_2/4$. We choose $r = 130$, $d_0 = 7$, $d_1 = 20$, $d_2 = 23$, and $l_1 = 95$, $l_3 = l_4 = l_{10} = l_9 = 77$. For segment 4 we choose $r = 50$ with all the same angles as for segment 1. See Figure 4 for the z -coordinates of each endpoint.

Appendix C. Small Rotations and Translations

Let $f(\mathbf{r})$ be a scalar function of the vector \mathbf{r} and let $\mathbf{r}' = \mathbf{R}^T(\mathbf{r} - \mathbf{r}_o)$. For infinitesimal rotations and translations we can write $\mathbf{r}' = \mathbf{r} - \delta\mathbf{r} - \delta\boldsymbol{\phi} \times \mathbf{r}$ where $\delta\mathbf{r}$ is an infinitesimal translation and $\delta\boldsymbol{\phi}$ is a vector giving the orientation of the axis of rotation and the magnitude of an infinitesimal angle of rotation about this axis. We want to approximate $f(\mathbf{r}')$ in terms of the ∇f and small translational and rotational variables. For $\mathbf{r}' = \mathbf{r} + \mathbf{d}$ we may always write:

$$f(\mathbf{r}') \approx f(\mathbf{r}) + \mathbf{d} \cdot \nabla f(\mathbf{r}) \quad (\text{C.1})$$

hence

$$f(\mathbf{r}') \approx f(\mathbf{r}) - (\delta\mathbf{r} + \delta\boldsymbol{\phi} \times \mathbf{r}) \cdot \nabla f(\mathbf{r}) \quad (\text{C.2})$$

which can be written as

$$f(\mathbf{r}') \approx f(\mathbf{r}) - \delta\mathbf{r} \cdot \nabla f(\mathbf{r}) - \delta\boldsymbol{\phi} \cdot \mathbf{r} \times \nabla f(\mathbf{r}). \quad (\text{C.3})$$

Therefore for small translations only we may write the time-varying net receive field as

$$C_{sos}(\mathbf{r}_p, t_n) \approx C_{sos}(\mathbf{r}_p, 0) - \delta\mathbf{r}(t_n) \cdot \nabla C_{sos}(\mathbf{r}_p, 0) \quad (\text{C.4})$$

where we have assumed that $\mathcal{A}^{-1}(0) = \mathcal{I}$, the identity operator.

References

- Arfken, G., 1985. *Mathematical Methods for Physicists*. Academic Press, New York.
- Bannister, P. R., Brady, J. M., Jenkinson, M., 2007. Integrating temporal information with a non-rigid method of motion correction for functional magnetic resonance images. *Image and Vision Computing* 25, 311–320.
- Cox, R. W., 1996. Afni: Software for analysis and visualization of functional magnetic resonance neuroimages. *Comput. Biomed. Res.* 29, 162–173.
- Friston, K. J., Ashburner, J., Frith, C. D., Poline, J. B., Heather, J. D., 1995. Spatial normalization and registration of images. *Hum. Brain Mapp.* 3, 165–189.

- Giovannetti, G., Viti, V., Liu, Y., Yu, W., Mittra, R., Landini, L., Benassi, A., 2008. An accurate simulator for magnetic resonance coil sensitivity estimation. *Concepts Magn. Reson.* 33B, 209–215.
- Griswold, M. A., Jakob, P. M., Heidemann, R. M., Nittka, M., Jellus, V., Wang, J., Kiefer, B., Haase, A., 2002. Generalized autocalibrating partially parallel acquisitions (grappa). *Magn. Reson. Med.* 47, 1202–1210.
- Hajnal, J. V., Myers, R., Oatridge, A., Schwieso, J. E., Young, I. R., Bydder, G. M., 1994. Artifacts due to stimulus correlated motion in functional imaging of the brain. *Magn. Reson. Med.* 31, 283–291.
- Hartwig, A., Engstrom, M., Flodmark, O., Ingvar, M., Skare, S., 2011. A simple method to reduce signal fluctuations in fmri caused by the interaction between motion and coil sensitivities. *Proc. Intl. Soc. Mag. Reson. Med.* 19, 3628.
- Jenkinson, M., Bannister, P. R., Brady, J. M., Smith, S. M., 2002. Improved optimisation for the robust and accurate linear registration and motion correction of brain images. *NeuroImage* 17, 825–841.
- Jezzard, P., Balaban, R. S., 1995. Correction for geometric distortion in echo planar images from b0 field variations. *Magn. Reson. Med.* 34, 65–73.
- Jin, J., 1989. *Electromagnetic Analysis and Design in Magnetic Resonance Imaging*. CRC Press, 1999.
- Kaza, E., Klose, U., Lotze, M., 2009. Comparison of bold-signal magnitude between a 32-channel and a 12-channel head coil. *IFMBE Proceedings* 25, 213–216.
- Kaza, E., Klose, U., Lotze, M., 2011. Comparison of a 32-channel with a 12-channel head coil: are there relevant improvements for functional imaging? *J Magn Reson Imaging* 34, 173–183.
- Kundu, P., Inati, S. J., Evans, J. W., Luh, W.-M., Bandettini, P. A., 2012. Differentiating bold and non-bold signals in fmri time series using multi-echo epi. *NeuroImage* 60, 17591770.
- Li, J., Wang, L., Wang, Y., 2009. Visual bold-fmri with 32 channel phased-array coil at 3.0T mri system: comparison with 12 channel coil. *Proc. Intl. Soc. Mag. Reson. Med.* 17, 1614.
- Muresan, L., Renken, R., Roerdink, J. B. T. M., Duifhuis, H., 2005. Automated correction of spin-history related motion artefacts in fmri: Simulated and phantom data. *IEEE Trans. Biomed. Eng.* 52, 1450–1460.
- Ogawa, S., Lee, T. M., Nayak, A. S., Glynn, P., 1990. Oxygenation-sensitive contrast in magnetic resonance image of rodent brain at high magnetic fields. *Magn Reson Med* 14, 68–78.
- Power, J. D., Barnes, K. A., Snyder, A. Z., Schlaggar, B. L., Petersen, S. E., 2011. Spurious but systematic correlations in functional connectivity mri networks arise from subject motion. *Neuroimage* 59, 2142–2154.
- Pruessmann, K. P., Weiger, M., Scheidegger, M. B., Boesiger, P., 1999. Sense: Sensitivity encoding for fast mri. *Magn. Reson. Med.* 42, 952–962.
- Reykowski, A., 2006. Design of dedicated mri systems for parallel imaging. In: Schnberg, S. O., Dietrich, O., Reiser, M. F. (Eds.), *Parallel Imaging in Clinical MR Applications*. Springer, pp. 155–159.
- Roche, 2011. A four-dimensional registration algorithm with application to joint correction of motion and slice timing in fmri. *IEEE Trans. Med. Imag.* 30, 1546–1554.
- Roemer, P. B., Edelstein, A., Hayes, E., Souza, P., Mueller, M., Harris, R. L., 1990. The nmr phased array. *Magn. Reson. Med.* 16, 192–225.
- Sheltraw, D., Deshpande, V., Trumpis, M., Inglis, B., 2012. Simultaneous reduction of two common autocalibration errors in grappa epi time series data. *ArXiv:1208.0972*.

- Smith, S., Bannister, P., Beckmann, C., Brady, M., Clare, S., Flitney, D., Hansen, P., Jenkinson, M., Leiboivici, D., Ripley, B., Woolrich, M., Zhang, Y., 2001. Fsl: New tools for functional and structural brain image analysis. Seventh Int. Conf. on Functional Mapping of the Human Brain.
- Van Dijk, K. R. A., Sabuncub, M. R., Buckner, R. L., 2012. The influence of head motion on intrinsic functional connectivity mri. *Neuroimage* 59, 431–438.
- Walsh, D. O., Gmitro, A. F., Marcellin, M. W., 2000. Adaptive reconstruction of phased array mr imagery. *Magn. Reson. Med.* 43, 682–690.
- Wiesinger, F., de Moortele, P. F. V., Adriany, G., Zanche, N. D., Ugurbil, K., Pruessmann, K. P., 2006. Potential and feasibility of parallel mri at high field. *NMR Biomed* 19, 368–378.
- Woods, R. P., Cherry, S. R., Mazziotta, J. C., 1991. Rapid automated algorithm for aligning and reslicing pet images. *J. Comput. Assist. Tomogr.* 16, 620–633.